Wang, W, Xu, Y, Li, Y, Sun, Y, Fielding, AJ, Iamprasertkun, P, Yang, J, Wang, B, Li, Q, Wu, M and Hu, H

Evaluation of the Impact of Conductive Additives on the EPR Spectra of Hard Carbon Anodes

Evaluation of the Impact of Conductive Additives on the EPR Spectra of Hard Carbon Anodes

Abstract

Hard carbon (HC) is one of the most promising anode materials for sodium ion batteries, however, the controversial issue of the different state of charges of sodium ions relative to the localized structure of HC remains a topic of debate, highlighting the importance of understanding the underlying scientific differences. Electron paramagnetic resonance (EPR) spectroscopy is a powerful technique for understanding the electronic structure, thereby revealing insights into the structural and chemical changes of carbon materials undergoing various physical and chemical processes that are undetectable by other conventional techniques. We utilize EPR as the primary technique to reveal the sodium storage process in different carbon structures, with a focus on studying the impact of conductive carbon, an essential additive, on EPR characterization. Due to the physical properties of stored sodium ions (e.g., ionic state, quasi-metallic state) and associated structural characteristics, there are measurable effects on the EPR signal, including the linewidth and lineshape. Further comparative results demonstrate that even small amounts of conductive carbon additives can profoundly alter ex-situ EPR analysis, with the impact varying depending on the type of additive used. Therefore, we recommend carefully considering the use of conductive carbon when employing highly sensitive characterization techniques (e.g., EPR) to study energy storage mechanisms.

Introduction

The rising use of fossil energy has spurred a push towards renewable sources due to escalating energy and environmental issues, with large-scale energy storage technology, particularly secondary batteries, crucial for stabilizing clean energy supply amidst fluctuation and intermittence[1]. Sodium ion batteries (SIBs) are attracting attention due to their abundant resources, low cost, extended lifespan, and enhanced safety features. Currently, the performance of SIBs is suboptimal, with the lackluster performance of anode materials serving as a persistent bottleneck hindering their commercial viability, presenting a challenging and pressing research issue within the realm of energy storage[2]. Among them, graphite is a carbon-based material with a regular layered structure. However, due to its narrow interlayer spacing and thermodynamic constraints, the graphite anode exhibits minimal sodium storage capacity[3]. For soft carbon materials, despite their more disordered structure and larger interlayer spacing compared to graphite, they demonstrate only a limited slope

capacity for sodium storage through adsorption[4]. Hard carbon (HC) materials, stand out for their erratic structure, typically featuring expanded interlayer spacing (exceeding 0.37 nm), smaller crystallite sizes, abundant defect sites, and a well-developed pore network[5]. Such structural properties provide numerous active sites for sodium ion storage, resulting in an exceptional specific capacity. Notably, apart from the sloping capacity portion similar to that of soft carbon in sodium storage curve, HC also possesses a plateau sodium storage capacity near the sodium desorption potential, significantly enhancing its practicality[6].

The investigation of the sodium storage mechanism is crucial for comprehending the structure-activity relationship of HC materials and directing the design and synthesis of HC materials. Nevertheless, the absence of a precise crystal structure model for HC has resulted in the ongoing debate surrounding the mechanism of sodium storage within this material[7]. During the sodium intercalation/deintercalation process in graphite lattice, a small and highly reversible expansion occurs, and the reversible shift of the (002) peak in X-ray diffraction (XRD) directly reflects the change in interlayer spacing (notably, the insertion of sodium between stacked graphene sheets in X-ray scattering results in narrowing of diffraction peaks and intensity reduction)[8]; high-resolution transmission electron microscopy (HRTEM) corresponding fast Fourier transform (FFT)[9] and the reversible displacement of broad peaks at $q \approx 1.6\text{-}1.8$ Å^{-1} in wide-angle X-ray scattering (WAXS)[10] also describes the changes in interlayer spacing caused by sodium ion intercalation/deintercalation. Also the negative charge's transfer to graphene layers with the insertion of alkali metal ions, occupancy of the π^* antibonding band leads to weakening and elongation of C-C bonds, resulting in a redshift and broadening of the G band in Raman spectra[11]. The surface adsorption of alkali metal ions without inducing lattice changes tends to restrict the breathing vibrations of sp^2 carbon rings at defects and edges of carbon layers, leading to a decrease in intensity of the D band in Raman spectra (e.g. the I_D/I_G ratio)[11]. Nano-pore scattering signal intensity in small-angle X-ray scattering (SAXS)[12] reflects contrast between nanoscale pores and electronic density in the carbon matrix, and reversible changes in nano-pore scattering intensity during sodium filling indicate that nano-pores act as reversible sodium storage sites. In addition to these techniques that reflect single sodium ion storage processes, ^{23}Na solid-state nuclear magnetic resonance (NMR) provides a comprehensive reflection of various sodium storage processes through different chemical shifts: sodium ions in the graphite region possessing higher ionic characteristics than those in micropores due to weaker interactions between sodium ions and graphene layers compared to interactions between sodium ions and pore surfaces, resulting in higher frequencies in NMR spectra[13]. The study of sodium storage mechanisms through the above-mentioned techniques reveals that different characterization methods possess similar or complementary functions. However, despite understanding multiple characterization methods, researchers currently do not have a unified

explanation for the sodium storage mechanism of HC. This is attributed to the intricate structure of HC anode materials, which restricts the available characterization methods to ascertain only partial facts, resulting in varying information and conclusions among different researchers. Consequently, there is a requirement for further fundamental scientific research and enhanced characterization technologies to elucidate the sodium storage mechanism of HC.

Electron paramagnetic resonance (EPR) spectroscopy, owing to its sensitivity to the magnetic moments of single electrons, facilitates the examination of electronic structure evolution in anode/cathode materials under different state of charge (SOC)[14]. Due to the different spectral characteristics representing distinct structural and/or chemical changes in materials, EPR spectroscopy has been successfully applied to carbon materials, providing documentation and analysis of energy storage mechanisms including intercalation, adsorption and deposition[13c, 15]. Chemical adsorption may not generate a signal, but it can consume the existing intrinsic EPR signal, originating from localized paramagnetic centers (such as dangling bonds and exposed nano-graphene edges)[16]. By acting as a bridge, ex-situ EPR has demonstrated a correlation between spin density (defect content) and reversible capacity, indicating that the reaction of lithium (and sodium) with localized paramagnetic centers (defect sites) in carbon materials reduces reversible capacity[16]. Defects play a crucial role in regulating different charge storage mechanisms of sodium ions (metallic cluster state or ionic state), with the dominant metal–metal interactions in defect-rich carbon layers storing sodium in a metallic cluster state (EPR signal with a broad signal and shoulder)[17]. Furthermore, free radicals like C-C•/C-N• signals contribute significantly to the adsorbed sodium capacity at low potentials (<0.1V) during sodiation-desodiation processes in HC[18]. The delocalization of π electrons in graphite microcrystals induced by sodium ion intercalation between graphene layers manifests as broad Lorentzian lineshape EPR signals. Notably, sodium ion intercalation does not occur for graphene interlayer spacings less than 0.36 nm, and sodium ion intercalation for graphene interlayer spacings greater than 0.40 nm may be considered as the adsorption process[19]. The EPR spectral line shape of a metal conductor with a thickness d is primarily influenced by the finite penetration depth δ of the microwave field. When $d > \delta$, only spins within the skin depth are stimulated by the microwave field, giving rise to an asymmetric Dysonian lineshape. Conversely, if $d < \delta$, all electron spins are uniformly affected by the microwave field, resulting in a symmetric Lorentzian EPR signal. The "filling" phase from delocalized electrons in metallic clusters leads to sharp Lorentzian EPR lineshapes[13c, 20]. With symmetric Lorentzian lineshapes, sharp signals according to the skin effect, it indicates that the size of metal sodium clusters is very small at the nanoscale, which is distinct from the asymmetric Dysonian lineshape signals typically observed for HC electrodes with large-sized blocky metals formed on the surface of after over-discharge[17, 21]. Therefore, based on the EPR spectra (generation of new signals,

changes in linewidth and *g* value, etc., obtainable through deconvolution) and variations in spin properties (Pauli or Curie-Weiss law behavior), a correlation between different structural characteristics of carbon materials and electrochemical performance metrics is possible establish[22]. In line with the aforementioned criteria, ex-situ EPR has become a powerful tool for elucidating different storage mechanisms of metal ions and understanding the fundamental science behind them. Nonetheless, when leveraging EPR technology to probe the sodium storage mechanism in HC, researchers sometimes overlook minor experimental details.

The conductive additive is a critical component of the battery, having a significant impact on the overall performance[23]. Typically, the content of the conductive additive by weight is relatively low, with commercial formulations ranging between 3-6 wt%, while academic environments may see higher proportions being used (ca. 10 wt%)[24]. Particularly in certain in-situ experiments, the quantity of conductive carbon additives is frequently augmented to enhance the electrochemical performance of the in-situ apparatus, owing to the specific design of the device[25]. It is noteworthy that in characterization tests including XRD and Raman spectroscopy, the incorporation of conductive carbon does not exert an influence on the overall characterization outcomes. However, the intrinsic EPR signal of typical HC with a plateau capacity is quite weak[26], so even the addition of trace amounts of conductive carbon (which contains a large amount to defects due to large Brunauer-Emmett-Teller (BET) surface area) can introduce unnecessary complexities in the analyzing process. To date, there has been limited attention devoted to studying the influence of conductive additives on the EPR signal of carbon based anode materials, with only a few researchers briefly mentioning this aspect[27]. Here, to investigate the impact of conductive carbon additives on the EPR signal of HC anode materials, we chose two commonly used types of conductive carbon, namely Ketjen Black (KB) and Super-P (SP). Initially, we conducted a preliminary analysis of the influence of conductive carbon black on the EPR signals by examining the EPR spectrum of powder samples of individual conductive carbon black, original HC material, and HC material blended with conductive carbon black. Subsequently, we monitored and analyzed the charge and discharge processes of all samples using ex-situ EPR, attributing the sodium storage behavior of each component. Furthermore, we've emphasized the influence of the conductive additives on the EPR spectra during ex-situ testing processes. Our findings indicate that the inclusion of conductive carbon black can introduce deviations in the EPR spectrum analysis of HC materials, with varying effects based on the type of conductive carbon black used. These results hold significant implications for future investigations into the sodium storage mechanism of HC materials.

Results and Discussion

To validate the impact of incorporating conductive additives on the outcomes of traditional

characterization a series of tests was evaluated. Raman and XRD analyses were conducted on three distinct carbon samples, as well as on mixed samples (HC+KB, HC+SP, the ratio of HC to conductive additive was 9:1. It is noteworthy that an optimal content of conductive additive is essential for achieving enhanced discharge capacity and superior cycle performance. Inadequate content may result in fewer electron conduction pathways, hindering high current charging and discharging capabilities, whereas excessive content could lead to a decrease in the relative amount of active materials, consequently reducing battery capacity. Notably, a 10wt% dosage of conductive additive is commonly employed in academic research (Typically, electrodes are prepared by mixing 80 wt% HC, 10wt% conductive additive, and 10 wt% binder to form a slurry. However, this work only explores the influence of the addition of conductive additive on the original structural characteristics of HC under conventional characterization. Therefore, the binder was not added, and a simple mixture of powder form HC and conductive additive was used.). As depicted in **Figure 1a**, the Raman spectroscopy results (such as peak intensity and position) of the individual carbon materials exhibit significantly distinct spectrograms, while the mixed samples display almost congruent patterns. Further deconvolution of the Raman spectrum (**Figure S1** and **Table S1**) reveals comparable D_1/G and D_3/G values (The D_1/G peak area ratio can determine the degree of graphitization in the sample, while the D_3/G peak area ratio provides an indicator of oxygen functional group defects in the sample[22, 28]) among HC, HC+KB, and HC+SP, signifying similar levels of disorder and defect, which are notably different from KB and SP. Likewise, the XRD analysis findings (**Figure 1b**) indicate that the mixed samples exhibit a marginal deviation from the original HC sample, yet this variance does not compromise the assessment of overall structural characteristics. Examination of the XRD fitting results in **Table S2** further highlights the analogous half-peak width and d_{002} layer spacing of HC, HC+KB, and HC+SP, distinctly separate from KB and SP. These findings indicate that the presence of conductive carbon additives (after physical blending at a 10% ratio) does not significantly affect the overall results of traditional characterization tests, thereby ensuring the “accuracy” and “reliability” of the analytical outcomes. Consistently, the deconvolution results of XPS (**Figure S2**) confirm a similar trend to that of XRD and Raman spectroscopy.

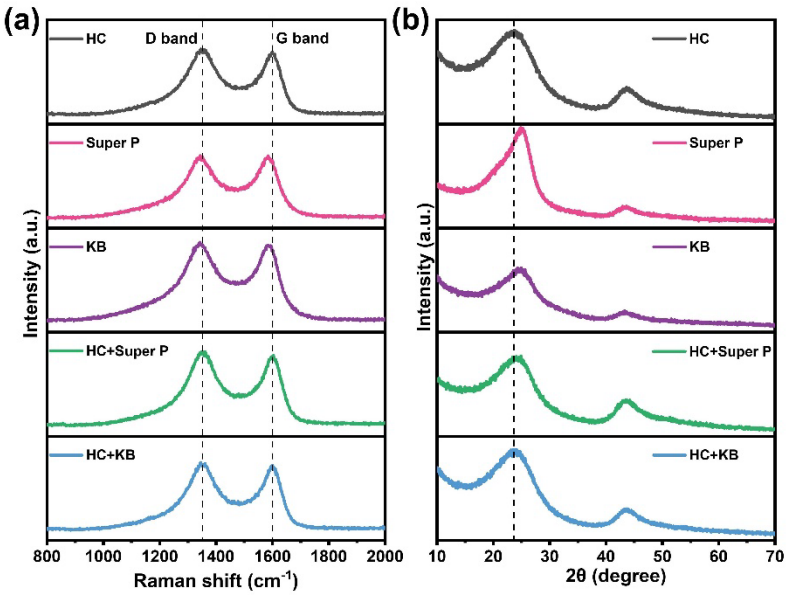

Figure 1. (a) Raman spectra and (b) powder XRD patterns of primary carbon samples and their mixtures.

The electrochemical performance of a sodium-ion half-cell utilizing three various carbon materials mixed with binder without conductive additives as anode materials was evaluated. **Figure 2** illustrates the galvanostatic charge-discharge (GCD) profiles for the initial three cycles. It is evident from the **Figure 2** that the electrochemical responses of the three carbon materials exhibit significant disparities due to its structural differences. Commercial HC materials exhibit a distinctive plateau capacity of sodium storage at low voltage level, with the highest initial coulombic efficiency (ICE) (78.4% for HC, 11.9% for KB, and 25.1% for SP) and specific capacity (201.8 mAh g^{-1} for HC, 141.2 mAh g^{-1} for KB, and 142.6 mAh g^{-1} for SP) among the three materials. Conversely, the GCD curves for the conductive carbon additives lack low-voltage plateau, showing a prolonged plateau corresponding to the formation of a solid-electrolyte interphase (SEI) between 1.5 V and 1.2 V in the first GCD cycle of SP and KB, which disappears in subsequent cycles. This phenomenon is attributed to the ultra-high specific surface area of the conductive carbon additives (specific surface area information is provided by the manufacturer and presented in **Table S3**), leading to substantial irreversible capacity during the initial charge-discharge process and consequently yielding a notably low ICE (around 10-30%). This trend is also evident in the cyclic voltammetry (CV) test results (**Figures S3** and **S4**), wherein the area of the second cycle of the CV curve for the conductive carbon additive significantly diminishes compared to that of the first cycle. Additionally, an observation in the low voltage range indicates a change in slope for both SP (below 0.1 V) and KB (below 0.2 V). This phenomenon may be attributed to variations in the adsorption process and changes in adsorption sites, leading to alterations in binding energy and consequently

influencing the slope in the lower voltage range[29].

Generally, the plateau capacity corresponds to that sodium ions are inserted between graphene layers or filled into closed pores. Based on XRD fitting results, the interlayer distance (d_{002}) of KB and SP is less than 0.36 nm (**Table S2**), suggesting the absence of sodium ion intercalation. Similarly, the SAXS test results (**Figure S8**) indicate the lack of a shoulder peak near 0.1 $Å^{-1}$ for KB and SP, implying the absence of closed pore structures and consequently, no pore-filling behavior by sodium ions[12, 30]. Hence, KB and SP exhibit a slope capacity primarily driven by adsorption, rather than intercalation or pore filling.

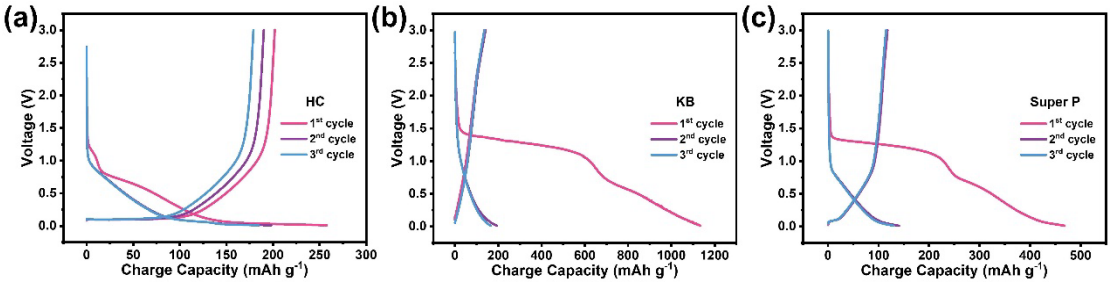

Figure 2. GCD curves of cycles 1-3 for (a) HC, (b) KB and (c) SP samples in the voltage window 3-0.01 V vs. Na^+/Na at 50 mA g^{-1}.

Given the aforementioned electrochemical process, we conducted ex-situ EPR analysis on three types of carbon batteries at different state of charges (SOCs). The pristine HC materials exhibits a broad EPR signal with the linewidth of 400.3 G and a *g* value ca. 2.002 (**Figure 3a**), signifying the presence of a considerable number of delocalized electrons in the infinite aromatic carbon structures[26]. Notably, the electrochemical tests conducted previously indicated that this specific HC material possesses a substantial plateau capacity, indicative of numerous closed pore structures, aligning with our prior findings. Additionally, the signal intensity from the broad signal is very weak, reflecting a very low content of defect structures in the HC. According to our prior work, the formation of plateau capacity requires the absence of many defects in the structure of HC, meaning there are not many delocalized electrons present (which may be associated with an imperfect carbon structure, such as dangling bonds at the edges of graphite microcrystals, functional groups), as an excessive presence of these defects would hinder the process of sodium ion filling or intercalation[16, 22].

In the case of the pristine KB material, its EPR response can be discerned into two distinct components through the line shape fitting (**Figure 3b**). A narrow signal was observed with a linewidth of 12.9 G and a *g* value ca. 2.003, which is attributed to localized spins, indicative of surface defects and various oxygen-containing functional groups as evidenced from the XPS characterizations (**Figure S2**)[22]. KB also displayed a broader signal (100 G) with *g* value around

2.002, consistent with conduction electrons within the limited aromatic hydrocarbon structure (limited aromatic framework (smaller L_a and L_c values, Tables S1 and S2) restricts the presence of delocalized electrons)[22, 26b]. Additionally, due to the larger specific surface area and pore size of the KB material, it falls short of creating a closed pore structure akin to HC materials, resulting in sodium storage in KB being predominantly governed by surface adsorption. Dissimilarly, the EPR signal of pristine SP manifests as two sharp narrow signals upon fitting (**Figure 3c**), representing distinct free radical environments characterized by localized electrons, possibly originating from the edges of the graphene layer and surface defects in the graphene layer[15a, 31]. Analogous to the KB material, SP, with its specific surface area and defect content, demonstrates a sodium storage mechanism primarily driven by sodium ion adsorption.

In the ex-situ EPR spectrum of HC anode without the conductive additive (**Figure 3a**) under different SOCs, two distinct components are identified (distinct linewidth), indicating that sodium was stored within different carbon structures. Taking into account the various sodium storage mechanisms in hard carbon, we hypothesize that the narrow signal is likely associated with metalloid sodium inserted or filled within the HC materials[13c, 17, 20, 31]. The broad signal can be attributed to sodium adsorption on the surface of carbon materials, originating from the carbon skeleton's delocalized electrons during charge transfer in electrochemical sodium storage[15b, 20]. Based on the preceding GCD curve, this HC material exhibits a significant plateau capacity, indicative of sodium ion filling into the closed pores or/and intercalation within graphene layers. This observation further corroborates our interpretation regarding the dual components seen in the EPR signal. These two modes of sodium storage are substantiated by the results of the SAXS analysis (**Figure S8**, with a notable shoulder peak around 0.1 $Å^{-1}$, indicative of a closed-cell structure) and XRD data (**Table S2**, the interlayer spacing of this HC material is approximately 0.376 nm, enabling sodium ion intercalation).

Notably, both conductive carbon materials exhibit distinct EPR signals from HC materials, underscoring variations in their sodium storage behaviors. In the case of KB (**Figure 3b**), only a sharp narrow signal around 2.4 G (g value ca. 2.003) is observed during the storage and extraction of sodium ions. Although the position and linewidth of this EPR signal are similar to that of quasi-metallic sodium in HC materials, based on the previous characterization results, KB material lacks closed pore structures required for filling and sufficient graphene interlayer spacing required for intercalation or filling. According to literature[15b], we attribute this signal to the adsorption process of sodium ions, which matches well with the GCD curve. This suggests that sodium storage in terms of KB primarily occurs in ionic states, including adsorption on defects or surfaces of graphene sheets[22, 31].

The ex-situ EPR spectrum of SP material can be identified as two distinct components (**Figure**

3c), representing different sodium storage processes, but unlike HC materials, both components exhibit narrow signals. The narrow signal has the identical *g* value (around 2.0023) as the EPR signal of KB, maintains a consistent linewidth throughout the charging and discharging stages, suggesting an association with the adsorption behavior of sodium ions on the graphene sheet surface. Given the resemblance of SP to KB, lacking the requisite conditions for sodium ion filling and intercalation. Therefore, according to the analysis of the GCD curve of SP, the broader signal could potentially stem from alterations in sodium ion adsorption sites, such as the adsorption at the edge of graphene layer[15a, 16]. Based on the ex-situ EPR findings above, the sodium storage behaviors of various carbon material structures exhibit stark disparities, clearly reflected in the EPR spectrum. Therefore, EPR proves to be a potent tool for investigating the sodium storage mechanisms across diverse carbon materials.

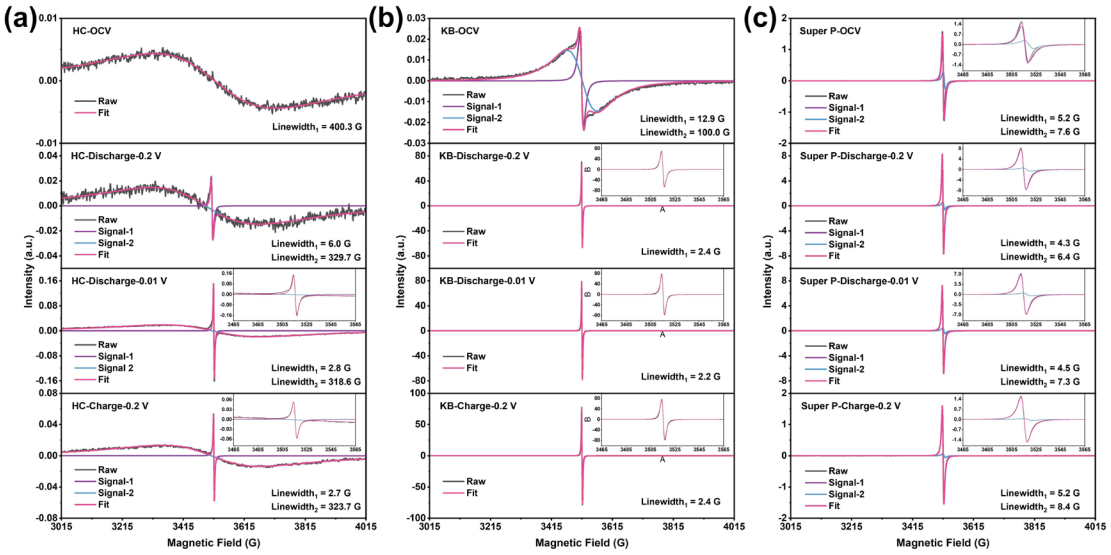

Figure 3. Ex-situ EPR spectra with simulated signals of (a) HC, (b) KB and (c) SP samples cycled in Na half-cells.

Upon electrochemical evaluation, it is evident that without the inclusion of conductive carbon additives, the reversible capacity, cycle performance, and rate capability of HC materials, particularly the commercialized HC materials, fall notably short of literature-reported values (**Figure S9**). However, upon addition of conductive carbon additives, a marked enhancement in sodium storage capacity, electrochemical stability, and rate capability is observed (**Figure 4** and **Figure S10**), aligning closely with literature benchmarks[32]. This improvement can be attributed to the intrinsically poor conductivity of HC materials, necessitating the incorporation of conductive carbon additives in electrode fabrication to bolster their electrochemical performance. Notably, the plateau capacity and slope capacity of HC materials show improvements to some extent after the

addition of conductive carbon additives, with KB demonstrating more pronounced effects than SP in enhancing the overall sodium storage capacity and rate performance of HC materials (**Tables S4** and **S5**).

Figures S9 and **S10** depict the rate performance curves of different anode samples from 0.01C to 0.5C (1C = 1000 mA g^{-1}). As expected, among all samples, the standalone HC sample exhibits the poorest rate performance (**Figure S9**). The addition of conductive additives not only leads to an increase in specific capacity but also demonstrates a significant advantage under high-rate conditions. The capacity retention of HC at 0.5C is 19.2%, while the capacity retentions of KB, SP, HC+KB, and HC+SP are 35.4%, 45.7%, 26.7%, and 26.0%, respectively. **Table S5** summarizes the contributions of the slope and plateau capacity at different C rates for various samples. Clearly, the rate performance of the plateau capacity component is the worst, with no significant plateau capacity observed at 0.2C and 0.5C. In contrast, the slope region exhibits better rate capabilities, attributed to different energy storage mechanisms associated with varying capacities. The slope region primarily involves surface-controlled processes, such as surface physical adsorption of sodium ions and chemical adsorption of defect structures. On the other hand, the plateau region corresponds to sodium ion intercalation and pore filling processes, primarily influenced by the diffusion rates of sodium ions within the turbulent layer and pores. The diffusion rate of sodium ions in HC materials is limited, impeding the effective utilization of plateau capacity under high current conditions. Additionally, kinetic analyses were conducted, with values of b for HC, HC+KB, and HC+SP in the low-voltage region being 0.75, 0.65, and 0.72, respectively (peak A, **Figures S5-7**), indicating sodium diffusion-controlled sodium storage processes. In the higher-voltage region, the b values for HC, HC+KB, and HC+SP obtained from CV curves (**Figures S5-7**) at different scanning rates (0.1 to 1.2 mV s^{-1}) are 0.89, 0.98, and 1.0, respectively (peak B, **Figures S5-7**), suggesting the presence of capacitive behavior. Assessing the contributions of diffusion and capacitance at different scan rates, it is noteworthy that the diffusion capacity decreases with increasing scan rate, consistent with the results of dQ/dV analysis (**Table S5**). Analysis of GCD and CV at different scan rates merely confirms the enhancement of HC performance by the addition of conductive additives. Disappointingly, the overall trend of electrochemical performance changes, whether conductive additives are added or not, is consistent, especially with minimal differences observed between the two materials with different conductive additives.

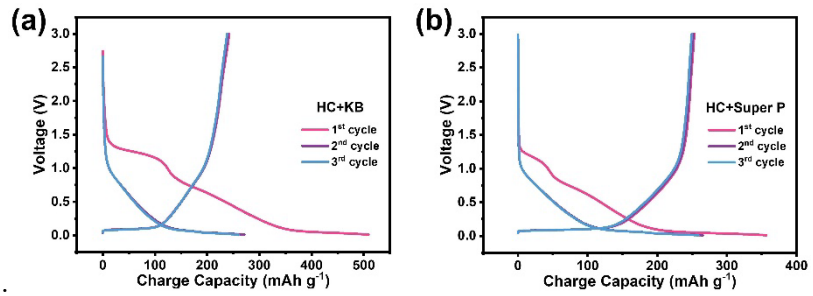

Figure 4. GCD curves of cycles 1-3 for (a) HC+KB and (b) HC+SP samples in the voltage window 3-0.01 V vs. Na^+/Na at 50 mA g^{-1}.

To discern the impact of conductive carbon additives on the sodium storage behavior of HC, further investigation was conducted into the alterations in ex-situ EPR spectra of HC materials in the presence of such additives. Strikingly, when the HC material was mixed with the conductive additive, a noticeable alteration in the EPR signal of the HC material itself was observed. Different from the single broad component of HC's EPR signal, a mixture of HC and KB results in the detection of two components with similar peak intensity yet distinct linewidths (a narrow and a broad signal) in the EPR signal (**Figure 5a**), and the *g* value (ca. 2.003) and linewidth (253.0 G) of the broad signal are distinctively different from those of HC signal (ca. 2.003) and linewidth (400.3 G). When blending samples with disparate signal intensities, there is a tendency for the weak and broad signal to be masked by super-strong and sharp one, potentially leading to its oversight during testing and analysis. When HC material is admixed with SP (as depicted in **Figure 5b**), a broad signal can still be discerned; however, this component's contribution to the overall signal diminishes significantly, rendering it challenging to distinguish through fitting.

The contrast between the ex-situ EPR spectrum of mixed samples and pure HC is more pronounced. In the case of HC+KB, the ex-situ spectrum can be identified as two narrow signals with similar *g* values. According to the GCD curve (**Figure 4a**), the HC mixed with conductive additives demonstrates both slope and plateau capacities, indicating the presence of both sodium ion adsorption and intercalation processes. Thus, the narrower signal (**Figure 5a**, Signal-1) with a larger linewidth may originate from the adsorbed sodium storage on the surface of the graphene sheet[22, 26b], and the broader signal (Signal-2) with a smaller linewidth may arise from the embedded sodium storage between graphene layers[17], while the broad signal originally belonging to HC (**Figure 3a**) disappears.

For HC+SP, the ex-situ spectrum exhibits two components akin to the ex-situ signal of HC: a narrow signal and a broad signal (**Figure 5b**). However, it is crucial to acknowledge that the intensity of the narrow signal in HC+SP surpasses that of the broad signal significantly, potentially leading to the oversight of the broad signal. Thus, care must be taken in the interpretation of the

EPR resonance.

Notably, even a mere 10% inclusion of conductive additives into HC materials elicited markedly divergent outcomes. Hence, even a minimal amount of conductive additive can exert a substantial influence on the spectral changes in EPR analysis. Because in-situ/ex-situ tests typically only involve the evaluation of the charge and discharge results of the initial one or two cycles, the discernible discrepancies in battery performance assessment with or without traditional conductive additives is not obvious (based on the electrochemical test results analyzed earlier). Therefore, in ex-situ/in-situ experiments, particularly in the configuration of carbon anode electrodes, the real behavior of the monitored samples can be more accurately reflected in EPR analysis without using conductive additives.

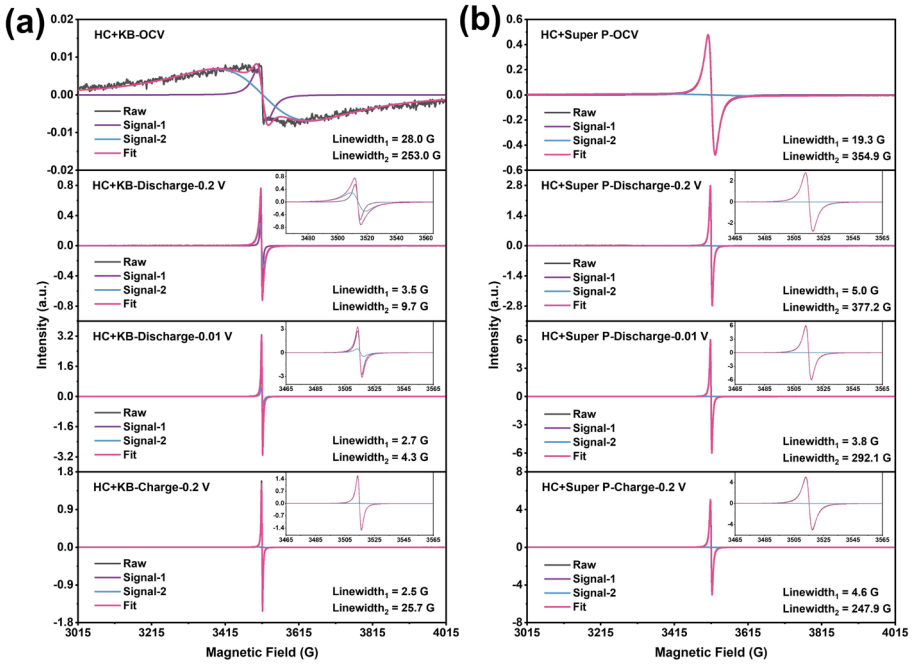

Figure 5. Ex-situ EPR spectra with simulated signals of (a) HC+KB and (b) HC+SP samples cycled in Na half-cells.

Conclusion

The EPR technique exhibits high sensitivity to the density of unpaired electron spins and environment, allowing for precise differentiation of electronic structure and associated sodium storage behaviors in different carbon materials. For instance, carbon materials exhibiting solely slope capacity (indicative of only sodium ion adsorption behavior) typically manifest as a single symmetrical narrow signal or can be deconvoluted into two narrow signals; whereas carbon materials displaying both capacitive slope and plateau capacities (signifying sodium ion adsorption as well as intercalation/filling behavior) commonly exhibit a symmetrical broad signal with a narrow

shoulder signal. Notably, even carbon materials of the same type and similar sodium storage processes may present notable discrepancies in their EPR spectra owing to variances in their electronic structures. Conductive additives are one of the most crucial components in batteries, and conductive carbon materials, particularly those with high specific surface areas, play a pivotal role in enhancing overall electrochemical performance. In some commonly used characterization techniques such as Raman and XPS, the addition of trace amounts of conductive additives does not alter the intrinsic properties of HC materials. However, through the utilization of ex-situ EPR techniques, we have discovered that even small amounts of conductive carbon additives, that is, the mixing of different carbon materials, can significantly impact EPR test results, leading to irreversible biases in the analysis and interpretation of findings. Consequently, we recommend avoiding the introduction of conductive additives when utilizing EPR in electrochemical investigations. Although foregoing lack of conductive additives may compromise the overall electrochemical response, this sacrifice is deemed acceptable for short-term ex-situ/in-situ analyses focusing on only the initial one or two cycles.

Methods

Material synthesis

The hard carbon materials were procured from a Japanese company, Wu Yu. The Ketjen black (KB) conductive additive was sourced from Dongguan Kelude New Energy Technology Co., Ltd., and the Super-P conductive additive was obtained from Shanghai Aowei Technology Development Co., Ltd. All of these materials were utilized as received without any further processing.

Material characterizations

The samples were subjected to X-ray diffraction (XRD) analysis using the X' Pert PRO MPD instrument from Panaco Company in the Netherlands at room temperature. The test conditions were set at kα = 1.5406, 40 kV, and I=150 mA. The average interlayer spacing was determined by applying Bragg's law.

$$2d_{002}\sin\theta_{002} = n\lambda$$

The c-axis crystallite sizes (L_c) was calculated as:

$$L_c = \frac{K\lambda}{\beta\cos\theta_{002}}$$

The Raman spectra of the materials were obtained using the laser confocal Raman spectrometer HR800 from the Horiba Jobin-Yvon Company in the United States, with an incident wavelength of 532 nm, 10% intensity, and a 50× objective lens. The spectrum was recorded for 10 seconds and

repeated three times for accumulation.

The a-axis crystallite size (L_a) of the HC samples was calculated according to the following equation:

$$L_a = \left(2.4\times10^{-10}\right)\lambda_{laser}^4\left(\frac{I_{D1}}{I_G}\right)^{-1}$$

All materials underwent X-ray photoelectron spectroscopy (XPS) analysis using the Thermo Fisher Scientific Company's X-ray photoelectron spectrometer (Escalab 250XI) under the conditions of Al Kα excitation and a spot size of 500μm.

Small-angle X-ray scattering (SAXS) measurements were collected on an Anton Paar SAXSpoint 2.0 with a Primux 100 microfocus sealed Cu tube source and 2D EIGER R HPC detectors for SAXS. Powdered samples were measured for approximately 20 min over the q-range $0.01 < q < 0.8$ Å^{-1}.

Electrochemical characterization

The anode active materials (HC, Super-P, or KB) and polyvinylidene fluoride (PVDF, Sigma) are blended in a 9:1 ratio, or a mixture of HC, a conductive additive (Super-P or KB), and PVDF are combined in an 8:1:1 ratio. The blend is dissolved in N-methyl-2-pyrrolidone (NMP) (anhydrous, >99.0%, Alfa Aesar) and then coated onto an aluminum foil. After complete drying at 80°C under vacuum, the aluminum foil coated with electrode material is cut into circular electrode pieces with a diameter of 1.2 cm.

The resulting electrode sheet serves as the working electrode, with a Na sheet as the counter electrode and reference electrode, and Whatman GF/D glass fiber as the diaphragm. A 1 M solution of $NaClO_4$ in an anhydrous organic solution of ethylene carbonate/diethylene carbonate (EC:DEC, 1:1 v/v%, battery grade, Saios) is utilized as the electrolyte.

The aforementioned components are assembled into a stainless steel CR2032 button cell within a glove box (Michelona (Shanghai) Industrial Intelligent Technology Co., Ltd.) filled with argon (O_2 and $H_2O \leq 0.1$ ppm), and electrochemical tests are conducted at room temperature. The galvanostatic charge/discharge (GCD) cycle test is performed within a voltage window of 3–0.01V vs. Na^+/Na and a current density of 50 mA g^{-1}. Cycling voltammetry (CV) measured by potentiostat (IVIUM-n-STAT) was carried out in the voltage window 3–0.01 V *vs.* Na^+/Na at a scan rate of 0.1 mV s^{-1}. Rate performance testing is conducted within the voltage window of 3–0.01 V vs. Na^+/Na under different current densities (10 mA g^{-1} to 500 mA g^{-1}). The GCD cycles and rate performance tests are executed using the battery cycler (NEWARE BTS-5 V).

EPR spectroscopy

EPR spectra were obtained at room temperature using a continuous wave (CW) Bruker EMXplus spectrometer operating at a microwave frequency close to 9.8 GHz, modulation amplitude

of 1 G, microwave power of 2.0 mW, and a receiver gain of 30 dB. An average spectrum was generated after twenty repeated scans.

For ex-situ EPR measurements, the electrode slurry (consisting of the anode active material HC, Super-P, or KB mixed with PVDF at a ratio of 9:1, or a mixture of HC, a conductive additive Super-P or KB, and PVDF at an 8:1:1 ratio) was dissolved in NMP and coated onto the diaphragm (Celgard 2325). The electrodes were cycled to various SOCs at a current density of 10 mA g^{-1}, and then the button cell was transferred to a glove box for removal of the electrode pieces, washing with ethyl carbonate (DEC, battery grade, Shanghai Aladdin Biochemical Technology Co., Ltd.), and drying in an argon-filled glove box at 50 °C (with O_2 and H_2O concentrations $\leqslant$ 0.01 ppm). Subsequently, the samples were sealed in EPR quartz tubes and removed from the glove box for data collection.

References

[1] a) W. Shu, J. Li, G. Zhang, J. Meng, X. Wang, L. Mai, *Nano-Micro Lett.* **2024**, *16*; b) Y. Wu, W. Shuang, Y. Wang, F. Chen, S. Tang, X.-L. Wu, Z. Bai, L. Yang, J. Zhang, *Electrochem. Energy Rev.* **2024**, *7*.

[2] a) Y. Gao, Q. Yu, H. Yang, J. Zhang, W. Wang, *Adv. Mater.* **2024**; b) C. Wu, Y. Yang, Y. Zhang, H. Xu, W. Huang, X. He, Q. Chen, H. Dong, L. Li, X. Wu, S. Chou, *Angew. Chem.-Int. Edit.* **2024**.

[3] Y. Yang, C. Wu, X.-X. He, J. Zhao, Z. Yang, L. Li, X. Wu, L. Li, S.-L. Chou, *Adv. Funct. Mater.* **2024**, *34*.

[4] C. Wu, Y. Yang, Y. Zhang, H. Xu, X. He, X. Wu, S. Chou, *Chem. Sci.* **2024**, *15*, 6244-6268.

[5] M. Zhang, Y. Li, F. Wu, Y. Bai, C. Wu, *Nano Energy* **2021**, *82*.

[6] Y. Chu, J. Zhang, Y. Zhang, Q. Li, Y. Jia, X. Dong, J. Xiao, Y. Tao, Q.-H. Yang, *Adv. Mater.* **2023**, *35*.

[7] X. Chen, C. Liu, Y. Fang, X. Ai, F. Zhong, H. Yang, Y. Cao, *Carbon Energy* **2022**, *4*, 1133-1150.

[8] a) J. Ding, H. Wang, Z. Li, A. Kohandehghan, K. Cui, Z. Xu, B. Zahiri, X. Tan, E. M. Lotfabad, B. C. Olsen, D. Mitlin, *Acs Nano* **2013**, *7*, 11004-11015; b) C. Cai, Y. Chen, P. Hu, T. Zhu, X. Li, Q. Yu, L. Zhou, X. Yang, L. Mai, *Small* **2022**, *18*; c) B. Zhang, C. M. Ghimbeu, C. Laberty, C. Vix-Guterl, J.-M. Tarascon, *Adv. Energy Mater.* **2016**, *6*.

[9] F. Sun, H. Wang, Z. Qu, K. Wang, L. Wang, J. Gao, J. Gao, S. Liu, Y. Lu, *Adv. Energy Mater.* **2021**, *11*.

[10] Y. Morikawa, S.-i. Nishimura, R.-i. Hashimoto, M. Ohnuma, A. Yamada, *Adv. Energy Mater.* **2020**, *10*.

[11] X. Chen, J. Tian, P. Li, Y. Fang, Y. Fang, X. Liang, J. Feng, J. Dong, X. Ai, H. Yang, Y. Cao, *Adv. Energy Mater.* **2022**, *12*.

[12] S. Komaba, W. Murata, T. Ishikawa, N. Yabuuchi, T. Ozeki, T. Nakayama, A. Ogata, K. Gotoh, K. Fujiwara, *Adv. Funct. Mater.* **2011**, *21*, 3859-3867.

[13] a) S. Alvin, H. S. Cahyadi, J. Hwang, W. Chang, S. K. Kwak, J. Kim, *Adv. Energy Mater.* **2020**,

10; b) J. M. Stratford, P. K. Allan, O. Pecher, P. A. Chater, C. P. Grey, *Chem. Commun.* **2016**, *52*, 12430-12433; c) S. Qiu, L. Xiao, M. L. Sushko, K. S. Han, Y. Shao, M. Yan, X. Liang, L. Mai, J. Feng, Y. Cao, X. Ai, H. Yang, J. Liu, *Adv. Energy Mater.* **2017**, *7*.

[14] a) D. T. Daniel, S. Oevermann, S. Mitra, K. Rudolf, A. Heuer, R.-A. Eichel, M. Winter, D. Diddens, G. Brunklaus, J. Granwehr, *Sci Rep* **2023**, *13*; b) J. R. Gonzalez, R. Alcantara, J. L. Tirado, A. J. Fielding, R. A. W. Dryfe, *Chem. Mat.* **2017**, *29*, 5886-5895; c) E. Sic, J. Rohrer, E. Ricohermoso, III, K. Albe, E. Ionescu, R. Riedel, H. Breitzke, T. Gutmann, G. Buntkowsky, *ChemSusChem* **2023**, *16*.

[15] a) I. Elizabeth, B. P. Singh, S. Trikha, S. Gopukumar, *J. Power Sources* **2016**, *329*, 412-421; b) E. Zhecheva, R. Stoyanova, J. M. Jiménez-Mateos, R. Alcántara, P. Lavela, J. L. Tirado, *Carbon* **2002**, *40*, 2301-2306; c) A. Diamantopoulou, S. Glenis, G. Zolnierkiwicz, N. Guskos, V. Likodimos, *J. Appl. Phys.* **2017**, *121*.

[16] R. Alcántara, G. F. Ortiz, P. Lavela, J. L. Tirado, *Chem. Mat.* **2006**, *18*, 2293-2301.

[17] Q. Li, J. Zhang, L. Zhong, F. Geng, Y. Tao, C. Geng, S. Li, B. Hu, Q.-H. Yang, *Adv. Energy Mater.* **2022**, *12*.

[18] Q. Gan, N. Qin, S. Gu, Z. Wang, Z. Li, K. Liao, K. Zhang, L. Lu, Z. Xu, Z. Lu, *Small Methods* **2021**, *5*.

[19] I. Escher, G. A. Ferrero, M. Goktas, P. Adelhelm, *Adv. Mater. Interfaces* **2022**, *9*.

[20] G. Liu, Z. Wang, H. Yuan, C. Yan, R. Hao, F. Zhang, W. Luo, H. Wang, Y. Cao, S. Gu, C. Zeng, Y. Li, Z. Wang, N. Qin, G. Luo, Z. Lu, *Adv. Sci.* **2023**, *10*.

[21] a) G. Feher, A. F. Kip, *Phys. Rev.* **1955**, *98*, 337-348; b) F. J. Dyson, *Phys. Rev.* **1955**, *98*, 349-359.

[22] B. Wang, J. R. Fitzpatrick, A. Brookfield, A. J. Fielding, E. Reynolds, J. Entwistle, J. Tong, B. F. Spencer, S. Baldock, K. Hunter, C. M. Kavanagh, N. Tapia-Ruiz, *Nat. Commun.* **2024**, *15*.

[23] a) J. C. Hestenes, J. T. Sadowski, R. May, L. E. Marbella, *ACS Mater. Au* **2023**, *3*, 88-101; b) J. Kang, L. Gu, J. V. Wang, Z. Wu, G. Zhu, Z. Li, *J. Power Sources* **2022**, *542*; c) X. Qi, B. Blizanac, A. DuPasquier, M. Oljaca, J. Li, M. Winter, *Carbon* **2013**, *64*, 334-340; d) L. Xu, W. Lv, K. Shi, S. Xiao, C. You, Y.-B. He, F. Kang, Q.-H. Yang, *Carbon* **2019**, *149*, 257-262; e) Y. D. Yucel, E. Adolfsson, H. Dykhoff, J. Pettersson, S. Trey, M. Wysocki, E. W. Zetterstrom, D. Zenkert, R. W. Lindstrom, G. Lindbergh, *Compos. Sci. Technol.* **2024**, *251*.

[24] T. Insinna, E. N. Bassey, K. Marker, A. Collauto, A.-L. Barra, C. P. Grey, *Chem. Mat.* **2023**, *35*, 5497-5511.

[25] a) K. Marker, C. Xu, C. P. Grey, *J. Am. Chem. Soc.* **2020**, *142*, 17447-17456; b) Q. Zhang, D. C. Bock, K. J. Takeuchi, A. C. Marschilok, E. S. Takeuchi, *J. Electrochem. Soc.* **2017**, *164*, A897-A901; c) J. Zhou, W. Ye, X. Lian, Q. Shi, Y. Liu, X. Yang, L. Liu, D. Wang, J.-H. Choi, J. Sun, R. Yang, M.-S. Wang, M. H. Rummeli, *Energy Storage Mater.* **2022**, *46*, 20-28.

[26] a) B. Wang, Y. Yao, W. Wang, Y. Xu, Y. Sun, Q. Li, H. Hu, M. Wu, *Chem. Eng. J.* **2024**, *488*; b) B. Wang, Y. Yao, W. Wang, Y. Xu, Y. Wan, Y. Sun, Q. Li, H. Hu, M. Wu, *J. Colloid Interface Sci.* **2024**, *664*, 681-690.

[27] K. A. See, M. A. Lumley, G. D. Stucky, C. P. Grey, R. Seshadri, *J. Electrochem. Soc.* **2017**, *164*, A327-A333.

[28] H. Moon, M. Zarrabeitia, E. Frank, O. Bose, M. Enterria, D. Saurel, I. Hasa, S. Passerini, *Batteries Supercaps* **2021**, *4*, 960-977.

[29] R. Guo, C. Lv, W. Xu, J. Sun, Y. Zhu, X. Yang, J. Li, J. Sun, L. Zhang, D. Yang, *Adv. Energy*

Mater. **2020**, *10*.

[30] D. A. Stevens, J. R. Dahn, *J. Electrochem. Soc.* **2000**, *147*, 4428.

[31] Z.-E. Yu, Y. Lyu, Y. Wang, S. Xu, H. Cheng, X. Mu, J. Chu, R. Chen, Y. Liu, B. Guo, *Chem. Commun.* **2020**, *56*, 778-781.

[32] a) E. M. Reynolds, J. Fitzpatrick, M. O. Jones, N. Tapia-Ruiz, H. Y. Playford, S. Hull, I. McClelland, P. J. Baker, S. A. Cussen, G. E. Perez, *J. Mater. Chem. A* **2024**; b) Z. Tang, S. Zhou, P. Wu, H. Wang, Y. Huang, Y. Zhang, D. Sun, Y. Tang, H. Wang, *Chem. Eng. J.* **2022**, *441*; c) Y. Wan, Y. Qiu, C. Wang, H. Zhang, Q. Zheng, X. Li, *J. Power Sources* **2021**, *496*.

Supporting Information

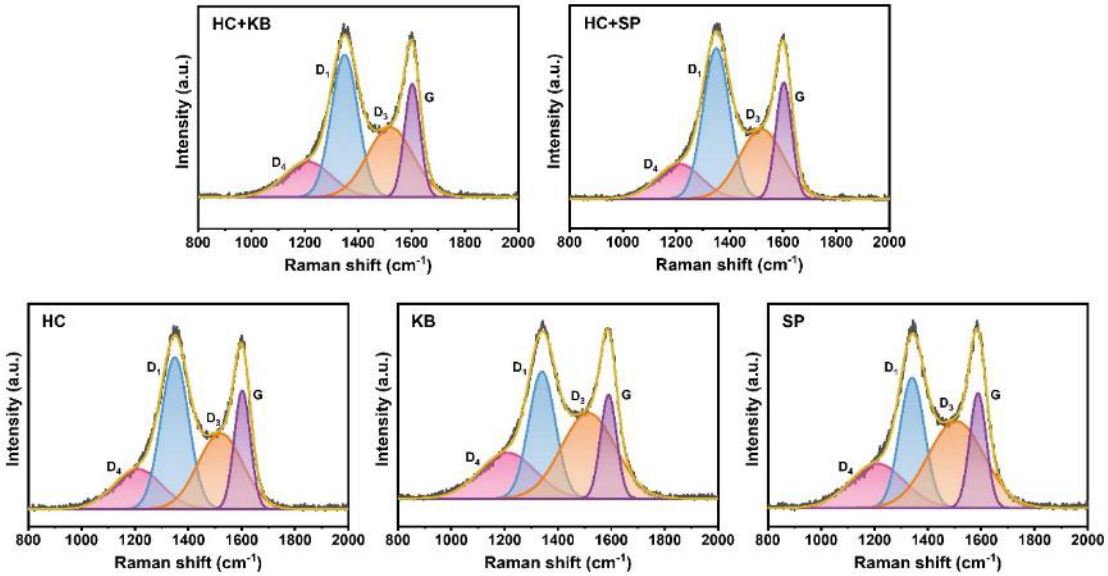

Figure S1. Raman spectra of HC+KB, HC+SP, HC, KB and SP simulated with four different components.

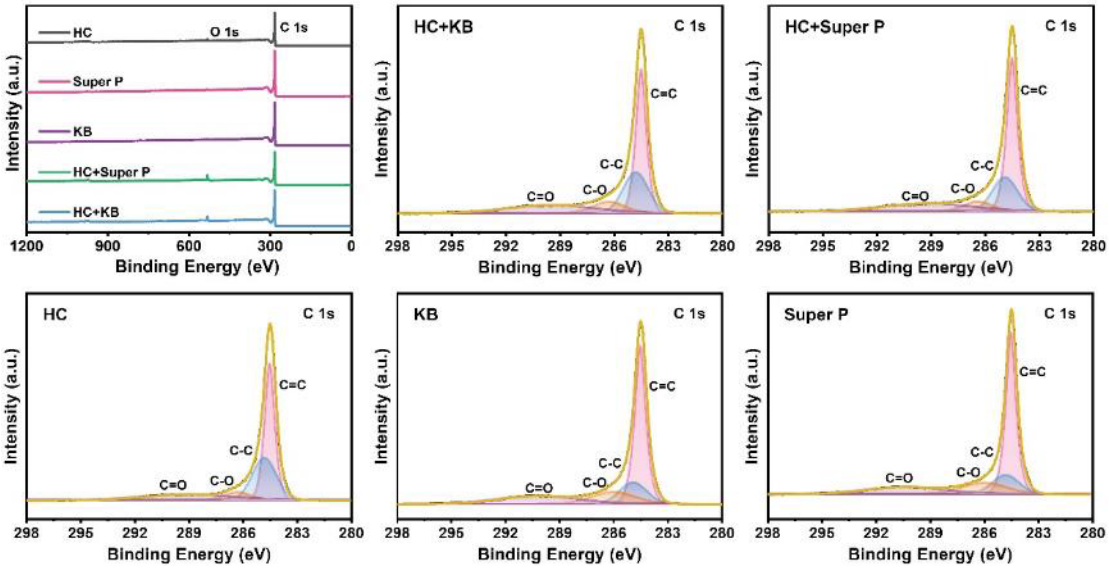

Figure S2. XPS survey spectra and high-resolution C1s spectra of primary carbon samples and their mixtures.

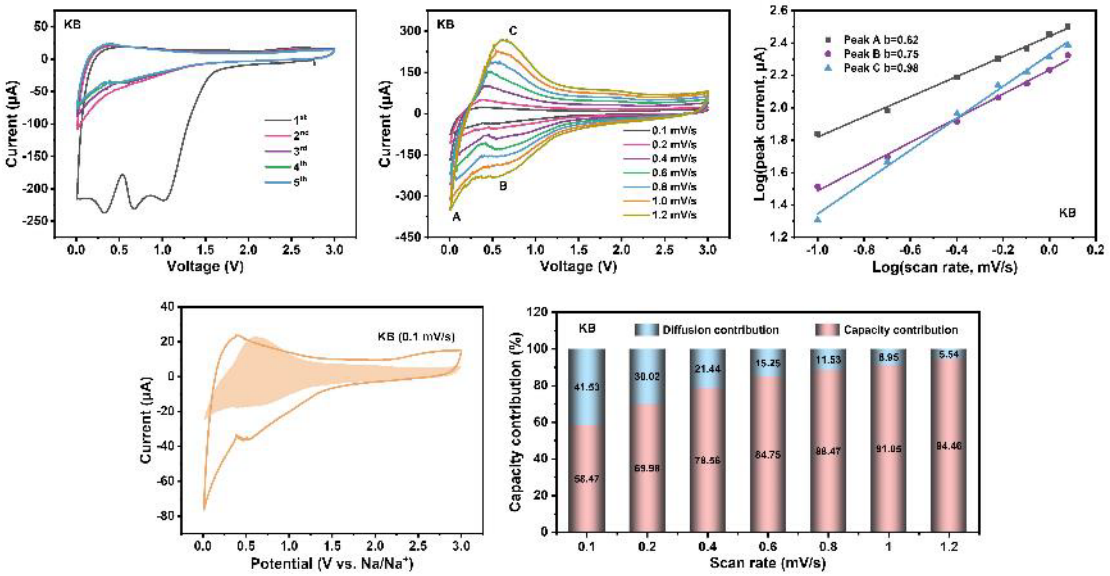

Figure S3. CV curves at 0.1 mV s^{-1}; CV curves at different scan rates; the fitted lines of ln(i) versus ln(v) plots in different oxidation and reduction states; the area comparison of capacitive contribution to total storage in CV at 0.1 mV s^{-1}; the contribution ratio of capacitance at different scan rates of the KB sample.

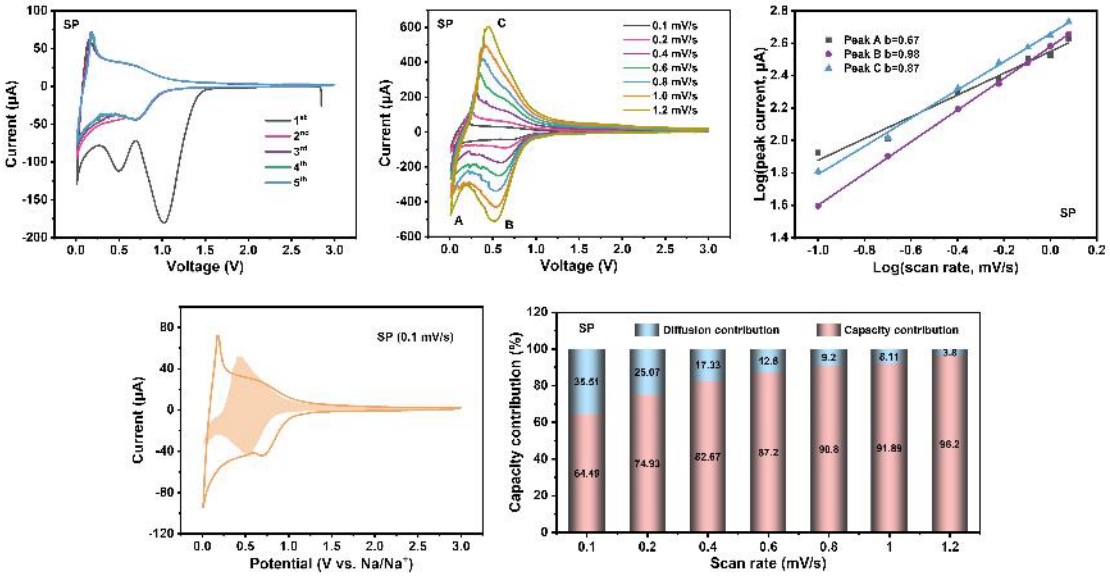

Figure S4. CV curves at 0.1 mV s^{-1}; CV curves at different scan rates; the fitted lines of ln(i) versus ln(v) plots in different oxidation and reduction states; the area comparison of capacitive contribution to total storage in CV at 0.1 mV s^{-1}; the contribution ratio of capacitance at different scan rates of the SP sample.

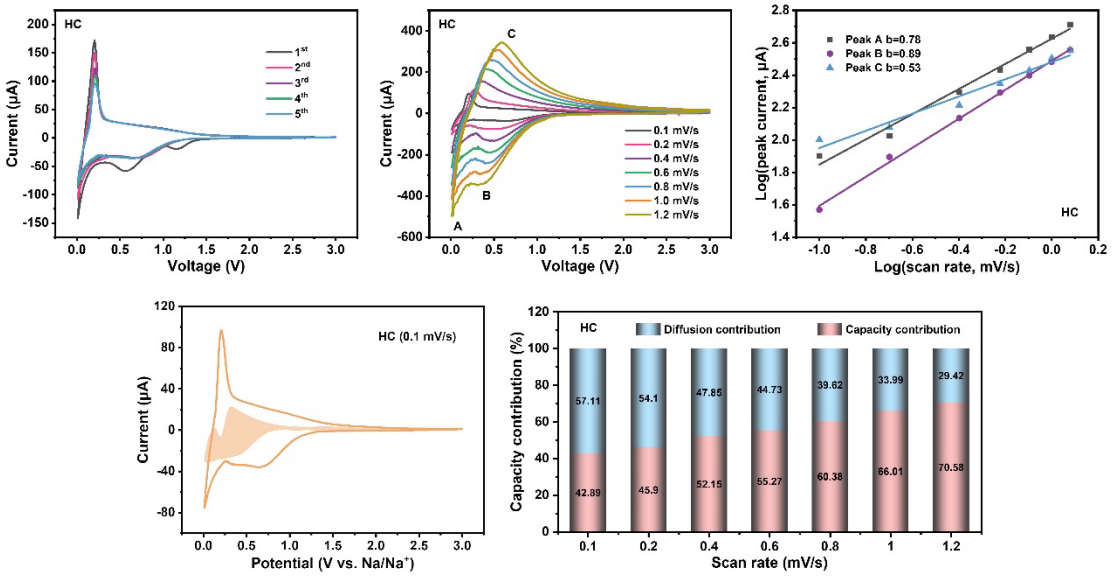

Figure S5. CV curves at 0.1 mV s^{-1}; CV curves at different scan rates; the fitted lines of ln(i) versus ln(v) plots in different oxidation and reduction states; the area comparison of capacitive contribution to total storage in CV at 0.1 mV s^{-1}; the contribution ratio of capacitance at different scan rates of the HC sample.

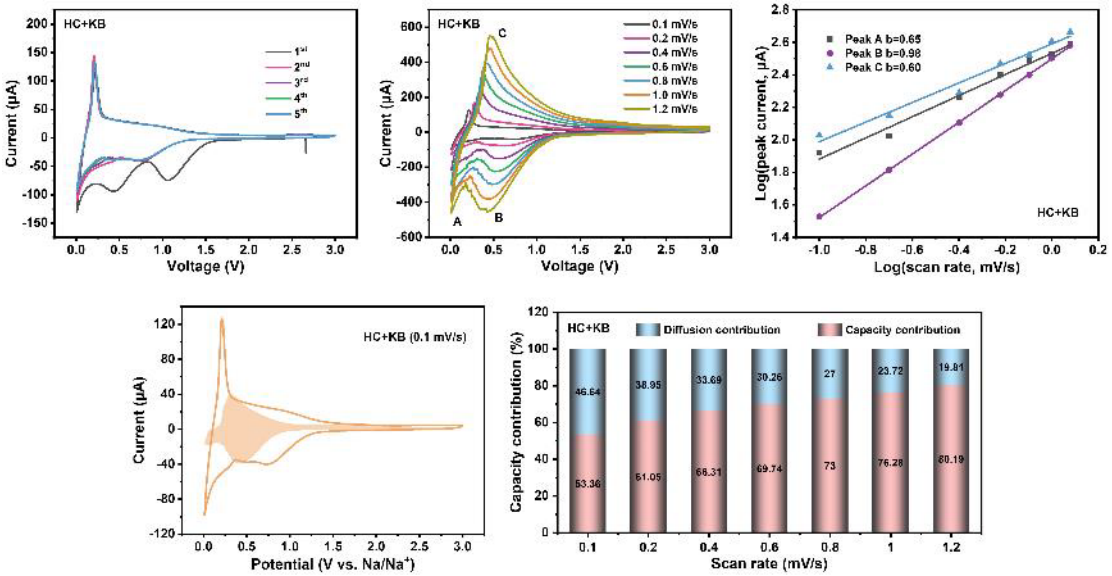

Figure S6. CV curves at 0.1 mV s^{-1}; CV curves at different scan rates; the fitted lines of ln(i) versus ln(v) plots in different oxidation and reduction states; the area comparison of capacitive contribution to total storage in CV at 0.1 mV s^{-1}; the contribution ratio of capacitance at different scan rates of the HC+KB sample.

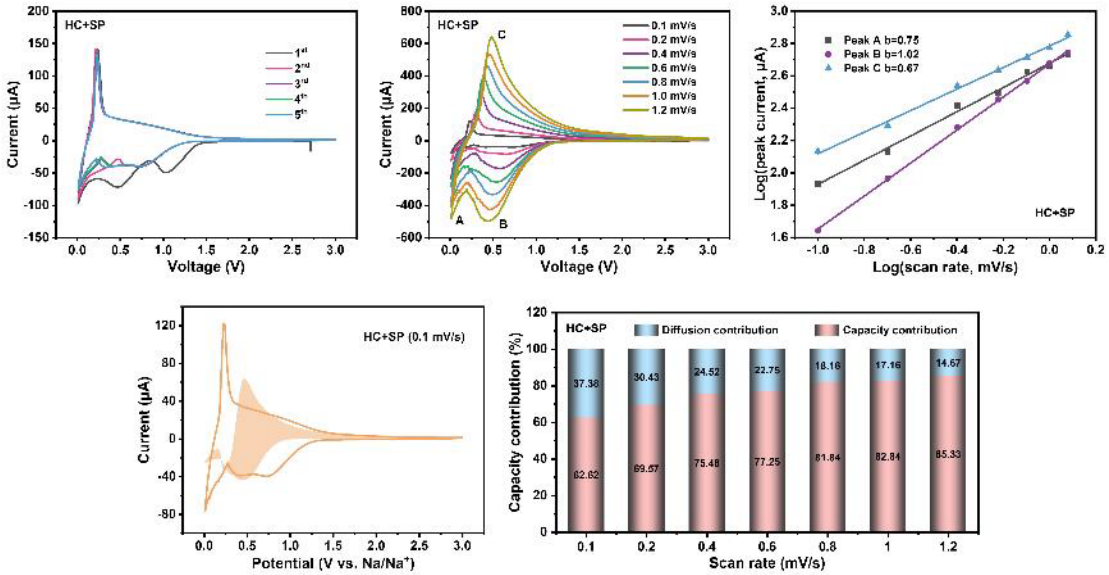

Figure S7. CV curves at 0.1 mV s^{-1}; CV curves at different scan rates; the fitted lines of ln(i) versus ln(v) plots in different oxidation and reduction states; the area comparison of capacitive contribution to total storage in CV at 0.1 mV s^{-1}; the contribution ratio of capacitance at different scan rates of the HC+SP sample.

Based on the CV curves acquired at various scan rates, the correlation between peak current (i) and scan rate (v) at a fixed voltage can be expressed by the equation:

$$i = av^b$$

$$\log(i)=\log(a) + b*\log(v)$$

In this equation, i represents the peak current in milliamperes (mA), v represents the scan rate (mV·s^{-1}), and a and b are adjustable coefficients. The value of parameter b can be divided into two ranges: when b tends to 0.5, it predominantly signifies a diffusion-controlled sodium storage mechanism, whereas a value approaching 1.0 indicates a predominance of capacitance-controlled processes.

The contribution of capacitance-controlled processes can be determined using the following equation:

$$i\,(\mathrm{V}) = k_1v+k_2v^{1/2}$$

Here, V represents the voltage of the battery (V), and k_1 and k_2 are adjustable parameters. To obtain the values of k_1 and k_2, we can divide both sides of equation by $v^{1/2}$, resulting in:

$$i\,(\mathrm{V})/v^{1/2} = k_1v^{1/2} + k_2$$

Subsequently, by plotting i(V)/$v^{1/2}$ as a function of $v^{1/2}$, we can determine the slope, which corresponds to the value of k_1. Furthermore, for each scan rate, we can plot the voltage (V) on the x-axis and k_1v on the y-axis, generating a graph that encloses a curve. The area enclosed by this curve represents the capacitance-based sodium storage capacity. By calculating the ratio of this area to the area under the CV curve at that specific scan rate, we can quantify the percentage contribution of capacitance to the overall sodium storage capacity at that particular scan rate.

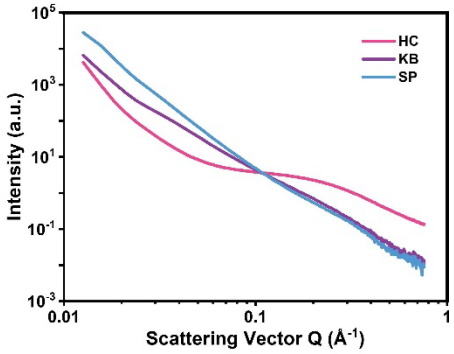

Figure S8. SAXS patterns of HC, KB, and SP.

Open and closed porosity in HC, KB, and SP were assessed using SAXS, where micropores and mesopores in the bulk can be detected due to differences in scattering density. SAXS patterns showed two domains: a first region in the $0.01 < q < 0.1$ Å^{-1} range, where there is a decrease in scattering intensity ca. 4th power of q from the scattering of the particle surface, followed by a second region with a plateau extending to $q = 0.1–0.3$ Å^{-1}, corresponding to the presence of micropores and nanometre-sized voids between sp^2 carbon planes.

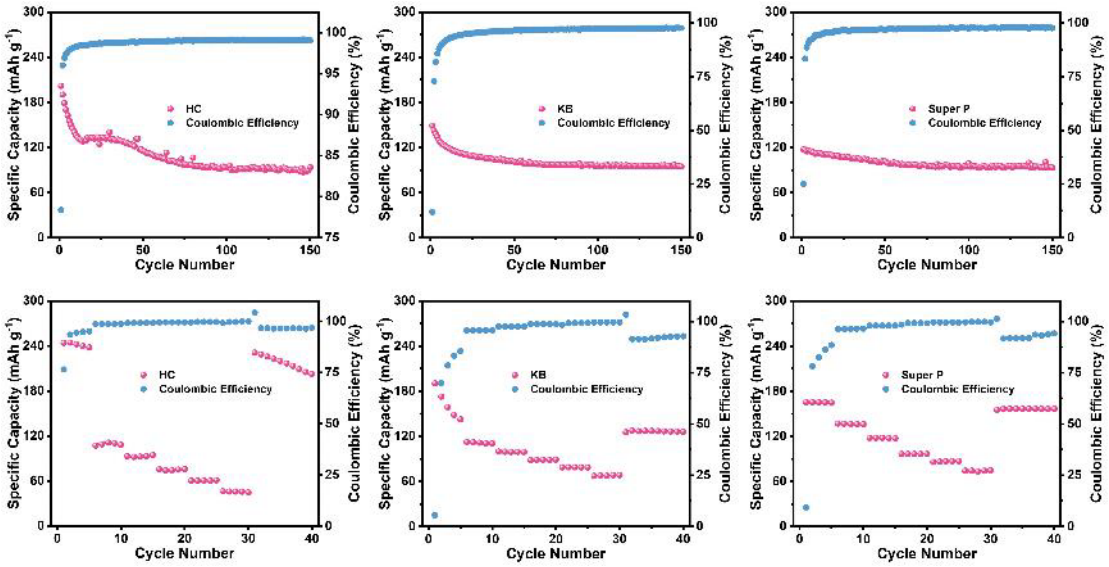

Figure S9. Cycling stability of HC, KB and SP samples with a current density of 50 mA g^{-1}. Specific capacities of HC, KB and SP samples under different current densities (10 mA g^{-1}, 30 mA g^{-1}, 50 mA g^{-1}, 100 mA g^{-1}, 200 mA g^{-1}, 500 mA g^{-1}, 10 mA g^{-1}).

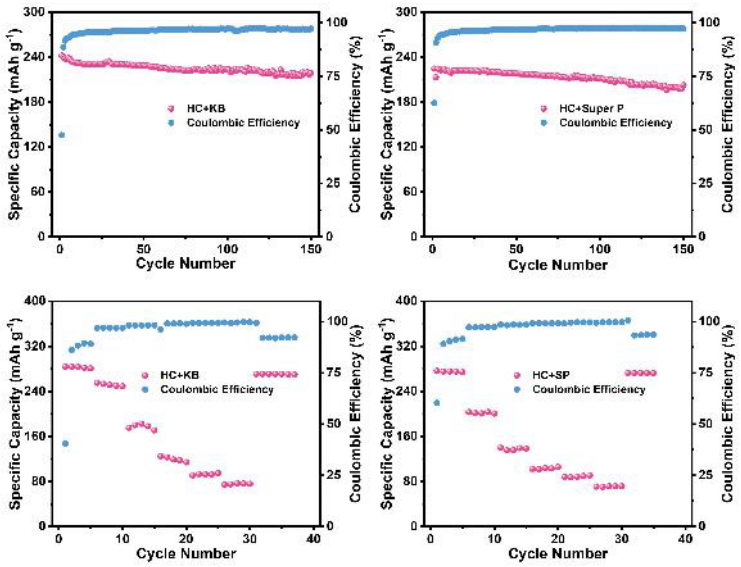

Figure S10. Cycling stability of HC+KB and HC+SP samples with a current density of 50 mA g^{-1}. Specific capacities of HC+KB and HC+SP samples under different current densities (10 mA g^{-1}, 30 mA g^{-1}, 50 mA g^{-1}, 100 mA g^{-1}, 200 mA g^{-1}, 500 mA g^{-1}, 10 mA g^{-1}).

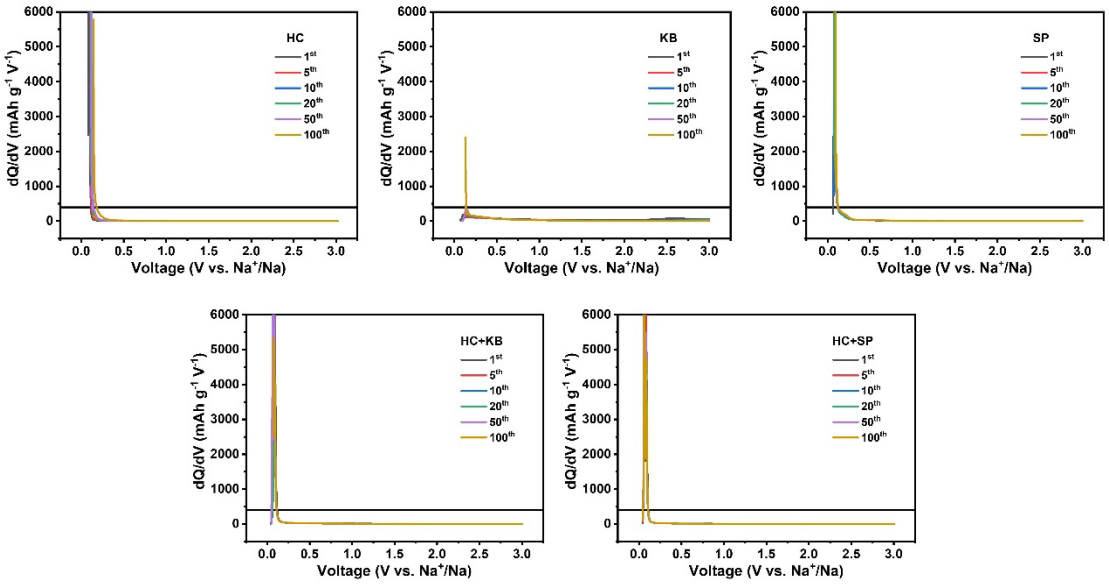

Figure S11. The dQ/dV plots of HC, KB, SP, HC+KB, and HC+SP at 50 mA g^{-1}.

The plateau processes were defined to start when dQ/dV < 400 mAh g^{-1} V^{-1} (labelled with a horizontal black line in the plots), following a similar approach to that reported in the literature.

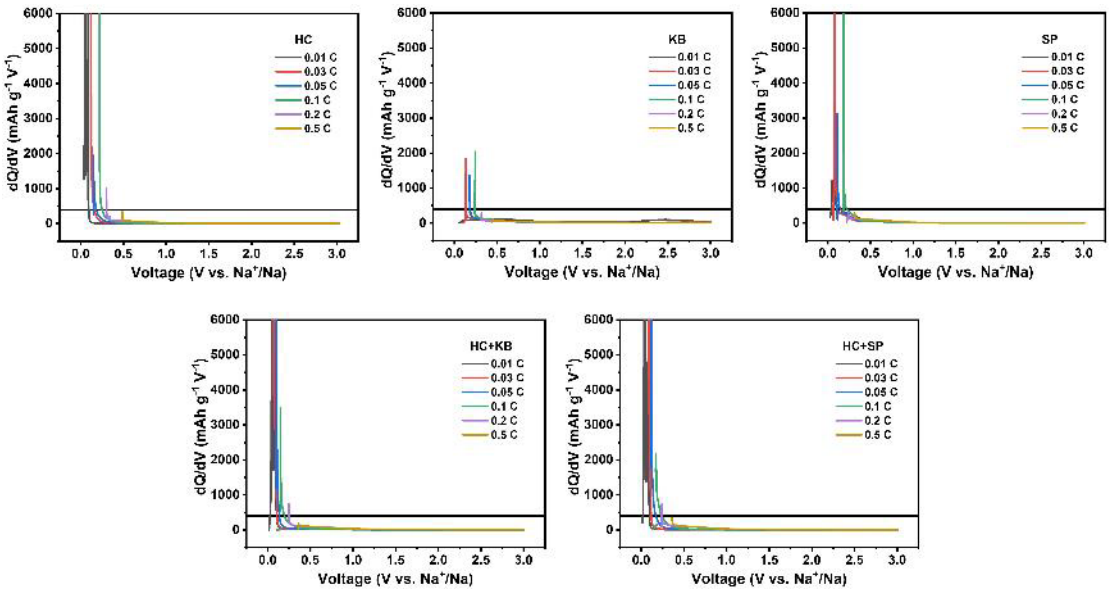

Figure S12. The dQ/dV plots of HC, KB, SP, HC+KB, and HC+SP at different C rates.

The plateau processes were defined to start when dQ/dV < 400 mAh g^{-1} V^{-1} (labelled with a horizontal black line in the plots), following a similar approach to that reported in the literature.

Table S1. Raman results of the HC, KB, SP, HC+KB, and HC+SP samples.

Sample	D_1/G	D_3/G	L_a/nm
HC	2.18	1.78	7.57
KB	2.02	2.76	8.16
SP	1.69	2.53	9.76
HC+KB	2.13	1.79	7.74
HC+SP	2.15	1.66	7.67

Table S2. XRD results of the HC, KB, SP, HC+KB, and HC+SP samples.

Sample	2θ	FWHM	d_{002}	L_c/nm
HC	23.68	7.41	3.75	1.08
KB	24.75	6.04	3.59	1.33
SP	25.02	4.96	3.56	1.62
HC+KB	23.94	7.36	3.71	1.09
HC+SP	24.09	6.86	3.69	1.17

Table S3. Brunauer-Emmett-Teller (BET) results of the HC, KB, and SP samples from manufacturers.

Sample	Manufacturer	BET (m^2/g)
Hard carbon	Kureha	48
Ketjen black	Lion Corporation	800
Super-P	TIMICAL	62

Table S4. The electrochemical properties of HC, KB, SP, HC+KB, and HC+SP at 50 mA g^{-1}.

		HC	KB	SP	HC+KB	HC+SP
1st	Charge capacity (mAh/g)	201.84	161.45	117.60	242.07	224.63
	Discharge capacity (mAh/g)	257.53	1208.63	468.53	509.09	358.94
	Coulombic efficiency (%)	78.37	13.36	25.10	47.55	62.58
	Plateau capacity (mAh/g)	83.31	——	22.74	95.30	93.99
	Slope capacity (mAh/g)	118.53	161.45	94.86	146.77	130.64
5th	Charge capacity (mAh/g)	162.39	134.25	114.98	238.75	222.72
	Discharge capacity (mAh/g)	166.26	151.53	125.13	256.77	235.78
	Coulombic efficiency (%)	97.67	88.59	91.89	92.98	94.46
	Plateau capacity (mAh/g)	58.13	——	20.81	95.72	92.18
	Slope capacity (mAh/g)	104.26	134.25	94.17	143.03	130.54
10th	Charge capacity (mAh/g)	135.85	123.06	112.14	232.32	221.16
	Discharge capacity (mAh/g)	138.23	132.60	118.79	245.41	231.76
	Coulombic efficiency (%)	98.28	92.81	94.40	94.67	95.42
	Plateau capacity (mAh/g)	41.02	——	19.85	92.75	93.20
	Slope capacity (mAh/g)	94.83	123.06	92.29	139.57	127.96
20th	Charge capacity (mAh/g)	132.40	113.34	108.54	230.84	221.82
	Discharge capacity (mAh/g)	134.29	118.91	112.74	241.53	230.50
	Coulombic efficiency (%)	98.59	95.32	96.28	95.57	96.24
	Plateau capacity (mAh/g)	39.92	——	18.06	92.75	94.69
	Slope capacity (mAh/g)	92.48	118.91	90.48	138.09	127.13
50th	Charge capacity (mAh/g)	115.29	103.79	101.27	228.34	217.91
	Discharge capacity (mAh/g)	116.57	106.98	104.61	237.02	225.05
	Coulombic efficiency (%)	98.91	97.02	96.81	96.34	96.83
	Plateau capacity (mAh/g)	29.63	1.39	14.34	91.91	92.44
	Slope capacity (mAh/g)	85.66	102.4	86.93	136.43	125.47
100th	Charge capacity (mAh/g)	93.00	99.67	98.83	228.63	211.91
	Discharge capacity (mAh/g)	93.83	101.84	101.59	234.84	217.53
	Coulombic efficiency (%)	99.11	97.87	97.29	97.36	97.42
	Plateau capacity (mAh/g)	17.11	0.70	13.92	92.76	88.65
	Slope capacity (mAh/g)	75.89	98.97	84.91	135.87	123.26

Table S5. The electrochemical properties of HC, KB, SP, HC+KB, and HC+SP at different C rates.

		HC	KB	SP	HC+KB	HC+SP
0.01C	Charge capacity (mAh/g)	244.02	190.40	165.55	284.04	276.66
	Discharge capacity (mAh/g)	318.94	3441.95	1761.60	700.14	458.79
	Coulombic efficiency (%)	76.51	5.53	9.40	40.57	60.30
	Plateau capacity (mAh/g)	108.25	——	19.89	117.51	120.50
	Slope capacity (mAh/g)	135.77	190.40	145.66	166.53	156.16
0.03C	Charge capacity (mAh/g)	111.07	112.66	136.97	255.42	203.42
	Discharge capacity (mAh/g)	112.51	117.85	142.31	263.30	208.72
	Coulombic efficiency (%)	98.72	95.59	96.24	97.01	97.46
	Plateau capacity (mAh/g)	26.18	2.57	20.00	104.96	73.01
	Slope capacity (mAh/g)	84.89	110.09	116.97	150.46	130.41
0.05C	Charge capacity (mAh/g)	94.40	99.63	117.78	182.51	138.81
	Discharge capacity (mAh/g)	95.13	102.15	120.25	185.96	140.93
	Coulombic efficiency (%)	99.24	97.54	97.95	98.15	98.50
	Plateau capacity (mAh/g)	17.48	1.94	12.79	57.75	34.14
	Slope capacity (mAh/g)	76.92	97.69	104.99	124.76	104.67
0.1C	Charge capacity (mAh/g)	75.95	88.49	96.71	124.82	105.95
	Discharge capacity (mAh/g)	76.29	89.65	97.56	125.88	106.74
	Coulombic efficiency (%)	99.55	98.72	99.13	99.16	99.26
	Plateau capacity (mAh/g)	10.83	1.94	9.72	22.78	18.87
	Slope capacity (mAh/g)	65.12	86.55	86.99	102.04	87.08
0.2C	Charge capacity (mAh/g)	60.88	78.78	87.12	94.64	90.65
	Discharge capacity (mAh/g)	61.05	79.29	87.57	95.11	90.94
	Coulombic efficiency (%)	99.73	99.36	99.49	99.51	99.68
	Plateau capacity (mAh/g)	2.78	——	——	3.89	4.44
	Slope capacity (mAh/g)	58.10	78.78	87.12	90.75	86.21
0.5C	Charge capacity (mAh/g)	46.94	67.35	75.70	75.87	71.93
	Discharge capacity (mAh/g)	46.94	67.65	75.98	76.01	72.08
	Coulombic efficiency (%)	99.99	99.57	99.63	99.82	99.78
	Plateau capacity (mAh/g)	——	——	——	——	——
	Slope capacity (mAh/g)	46.94	67.35	75.70	75.87	71.93